Article

Structure−Property Relationships for Nickel Aluminate Catalysts in Polyethylene Hydrogenolysis with Low Methane Selectivity

Brandon C. Vance, Sean Najmi, Pavel A. Kots, Cong Wang, Sungho Jeon, Eric A. Stach, Dmitri N. Zakharov, Nebojsa Marinkovic, Steven N. Ehrlich, Lu Ma, and Dionisios G. Vlachos*

Cite This: JACS Au 2023, 3, 2156−2165

Read Online

| ACCESS | Metrics & More | Article Recommendations | Supporting Information |

ABSTRACT: Earth-abundant metals have recently been demonstrated as cheap catalyst alternatives to scarce noble metals for polyethylene hydrogenolysis. However, high methane selectivities hinder industrial feasibility. Herein, we demonstrate that low-temperature ex-situ reduction (350 °C) of coprecipitated nickel aluminate catalysts yields a methane selectivity of <5% at moderate polymer deconstruction (25−45%). A reduction temperature up to 550 °C increases the methane selectivity nearly sevenfold. Catalyst characterization (XRD, XAS, ^{27}Al MAS NMR, H$_2$ TPR, XPS, and CO-IR) elucidates the complex process of Ni nanoparticle formation, and air-free XPS directly after reaction reveals tetrahedrally coordinated Ni^{2+} cations promote methane production. Metallic and the specific cationic Ni appear responsible for hydrogenolysis of internal and terminal C−C scissions, respectively. A structure-methane selectivity relationship is discovered to guide the design of Ni-based catalysts with low methane generation. It paves the way for discovering other structure−property relations in plastics hydrogenolysis. These catalysts are also effective for polypropylene hydrogenolysis.

KEYWORDS: plastics waste, nickel, earth-abundant metals, circular economy, catalyst restructuring
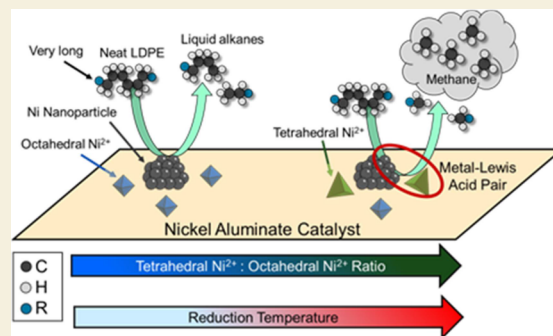
Plastics are ubiquitous in modern life. Global plastic production reached 460 Mt in 2019 and is projected to triple by 2060.[1] Approximately 99% of plastics are derived from fossil resources[2,3] and >90% of all plastics ever produced have been disposed of using dead-end methods (i.e., incineration, landfills, and the environment).[2] This linear (take, make, and waste) management model threatens global ecosystems[4,5] with major and not fully understood consequences stemming from micro- and nano-plastics.[6,7] Strategies must be developed to divert plastic waste (PW). Mechanical processes demand high polymer purity due to immiscibility between various plastics.[8] Few plastics are amenable to mechanical recycling, and grinding and crushing steps degrade the polymers' physical properties, eventually rendering the polymer unusable.[8] Subsequently, chemical deconstruction technologies must be developed.

Polyolefins (POs), such as polyethylene (PE) and polypropylene (PP), constitute ca. 57% of global plastic production[2] and are notoriously recalcitrant due to the stability of the C−H and C−C bonds. Numerous catalytic and noncatalytic methodologies have recently emerged to deconstruct POs. Hydrogenolysis,[9−18] hydrocracking,[19−21] and alkane metathesis[22,23] were demonstrated to convert POs to fuel, wax, and lubricant-ranged hydrocarbons, whereas acid cracking[24] and pyrolysis[25−27] produce a mixture of aliphatic, olefinic, and aromatic products. PO hydrogenolysis

is attractive due to its mild reaction temperatures and tunable product selectivity. Moreover, earth-abundant metals (i.e., Ni and Co) were recently demonstrated as viable alternatives to expensive noble metals (Ru, Pt, Rh, etc.).[14−16] Despite these advancements, both earth-abundant and noble metal-based catalysts generate significant fractions of undesired, low-value methane.[15,28] Mechanistic studies have elucidated methane is produced from internal C−C scission followed by fast terminal cascades.[13,15] Methodologies and active sites that can promote internal C−C scission while reducing the extent of terminal cascades are lacking.

Herein, we identify coprecipitated nickel aluminate (NiAl-T, where T denotes the reduction temperature) catalysts to be active for low-density polyethylene (LDPE) hydrogenolysis at moderate conditions (300 °C and 30 bar H$_2$). We demonstrate that lowering the ex-situ reduction temperature from 550 to 350 °C reduces the methane selectivity by nearly sevenfold (~33 to <5%) with limited impact on the liquid alkane (C$_6$−C$_{35}$) yields. Characterization of the NiAl-T identifies Ni atoms

2156

in cationic (Ni^{2+}) and metallic (Ni^0) states. Reduction redistributes Ni between cationic and metallic species and systematic experiments elucidate the process of generating Ni nanoparticles. Air-free XPS of the catalysts after reaction reveals restructuring of the surface and subsurface, dictated by the precursor state of the catalyst after ex-situ reduction. Post reaction characterization identifies a structure-methane selectivity relationship. These results highlight the role of the catalytic support and pairs of sites for activity and loss of selectivity while presenting a simple and easy method for reducing methane generation over Ni-based catalysts.

■ RESULTS

Characterization of NiAl-T Catalysts

Coprecipitated nickel aluminates are well-established catalysts for methane upgrading,[29−31] glycerol hydrogenolysis,[32,33] and other chemistries.[34−37] Synthesis by coprecipitation ensures that Ni is in close proximity to Al atoms by forming stoichiometric and nonstoichiometric nickel aluminates ($Ni_xAl_yO_z$).[30,32,37,38] Reduction of nickel aluminate at ≥350 °C with H_2 can generate metallic Ni nanoparticles on the support surface.[32−34,36] Strong interactions between Ni and Al prevent sintering of metal nanoparticles while tailoring the product selectivity.[30,32,37] Coprecipitated nickel aluminate catalysts were synthesized and reduced at 250−550 °C to gradually remove Ni from the proximity of Al and generate Ni nanoparticles with increasing reduction temperature (see Methods). Table 1 shows physical properties of the catalysts

Table 1. Summary of the NiAl-T Catalyst Characterization Including XRF, XPS, and N_2 Sorption

catalyst sample	bulk Al−Ni molar ratio (XRF)	surface Al−Ni molar ratio (XPS)	BET surface area (m²/g)	BJH average pore size (nm)
NiAl-250	2.4	9.0	233 ± 7	5.3
NiAl-350	2.0	9.1	243 ± 7	5.2
NiAl-450	1.8	10.5	246 ± 7	5.6
NiAl-550	1.9	10.2	190 ± 6	6.2

characterized by X-ray fluorescence (XRF), N_2 sorption, and X-ray photoemission spectroscopy (XPS). XRF shows that the catalysts have an Al−Ni molar ratio of 1.8:2.4, close to stoichiometric $NiAl_2O_4$. Sodium from precipitation was not detected by XRF.

Characterization by high-angle annular dark field scanning transmission electron microscopy (HAADF-STEM) coupled with elemental mapping via energy-dispersive X-ray spectroscopy (EDS) and electron energy loss spectroscopy (EELS) indicate both crystalline and amorphous phases across the NiAl-T catalysts. X-ray diffraction (XRD) identifies crystalline phases consisting of stoichiometric nickel aluminate ($NiAl_2O_4$), nickel oxide (NiO), metallic nickel (Ni), and alumina (Al_2O_3) (Figure S1). XRD only detected metallic Ni over NiAl-550 as nanoparticles of ~4.2 nm estimated from line broadening. Elemental mapping reveals that Ni is well-dispersed across the bulk for the NiAl-350 catalyst (Figure 1a), corroborating the incorporation of Ni into the solid lattice. The NiAl-450 (Figure S2) is practically identical to NiAl-350, but a tiny fraction of Ni nanoparticles was also detected, rationalizing the absence of metallic Ni peaks in the diffractograms. Conversely, an abundance of nanoparticles was observed in STEM of NiAl-550 (Figure 1b), with particle

diameters spanning 4.2 to 5.5 nm, coinciding with XRD results. Moreover, the formation and growth of Ni nanoparticles were directly observed on the calcined NiAl catalyst during in-situ reduction with H_2 using environmental transmission electron microscopy (ETEM). Ni nanoparticles of 5−7 nm were observed within 10 min of reduction at 550 °C (Figure 1c). Extending the reduction time to ~50 min resulted in nanoparticles of ~10−15 nm, which remained stable even at long time (>80 min).

X-ray absorption spectroscopy (XAS) in Figure 2a,b was employed to understand the crystal structure of the NiAl-250 catalyst. In X-ray absorption near edge spectroscopy (XANES), the K-edge for Ni (Figure 2a) has a strong white line at 8347 and 8351 eV, above the threshold energy, E_0, by 1.4 and 5.4 eV, respectively. Standard samples reveal that these spectral features are similar to $Ni(OH)_2$, where Ni is bound in an octahedral NiO_6 coordination sphere. The extended X-ray absorption fine structure (EXAFS) of NiAl-250 (Figure 2b) shows two equally intense peaks of Ni-O scattering pathways at ~1.63 Å in the first coordination sphere and Ni−Ni or Ni−Al in the second coordination sphere at ~2.61 Å. A standard of stoichiometric nickel aluminate ($NiAl_2O_4$) does not have an intense peak for the second shell, indicating a substantial contribution of Ni−Ni in the NiAl-250 sample, likely from partial Ni clustering. Furthermore, similarities in the EXAFS spectra for NiAl-250 and $Ni(OH)_2$ suggest that Ni is structured as stacked NiO_6 layers in the coprecipitated catalyst, similar to the hydroxide structure.

[27]Al magic angle spinning nuclear magnetic resonance (MAS NMR) measurements can reveal the coordination of the Al centers in heterogeneous catalysts.[39] ^{27}Al NMR spectra of the catalysts are shown in Figure 2c. Tetrahedral Al (Al_{Td}) resonates at a chemical shift of 68 ppm and octahedral Al (Al_{Oh}) resonates at 8.8 ppm for NiAl-250. There is no pentahedral Al species detected for all samples. For NiAl-350, the Al_{Td} shifts to 66 ppm indicating migration of the Ni away from tetrahedral positions toward octahedral positions.[40] The Al_{Oh} also shifted from 8.8 to 7.8 ppm, indicating a new Al environment due to Ni migration. NiAl-550 shows a shift in the Al_{Oh} from 7.8 to 11 ppm due to deshielding[41] from the migration of the Ni^{2+} species within the alumina matrix into Ni nanoparticles. This migration is common for metal-supported catalysts and indicates creation of harder to reduce supported species.[40]

The NiAl-T catalysts were characterized by air-free XPS, as shown in Figure 2d. The spectra are similar to previous reports.[31,34,42] Two main bands were observed at ~861 and ~855 eV corresponding to the Ni shakeup satellite and the Ni $2p_{3/2}$ peak, respectively. The Ni $2p_{3/2}$ peak was deconvoluted into three contributions assigned to nickel cations in $[NiO_6]$ octahedral centers that strongly interact with nearby Al (Ni^{2+}_{Oh}) at 855.7 eV; nickel cations in tetrahedral centers $[NiO_4]$ that weakly interact with nearby Al (Ni^{2+}_{Td}); and metallic nickel (Ni^0) at 852.1 eV.[29,33,34] Ni^{2+}_{Oh} and Ni^{2+}_{Td} comprise 81−100% of the Ni $2p_{3/2}$ peak across all catalyst samples with Ni^0 only appearing as a small shoulder on the NiAl-450 and 550 catalysts. Deconvolution of the NiAl-250 and 350 spectra indicate a redistribution of nickel cations from Ni^{2+}_{Td} to Ni^{2+}_{Oh} sites, likely minimizing the strain and free energy of the multicrystalline solid surface. The distribution of cationic nickel is significantly disturbed upon reduction at 450 °C, evidenced by an increase in the Ni^{2+}_{Td} contribution and a small fraction of Ni^0. This growth in the Ni^{2+}_{Td} contribution is
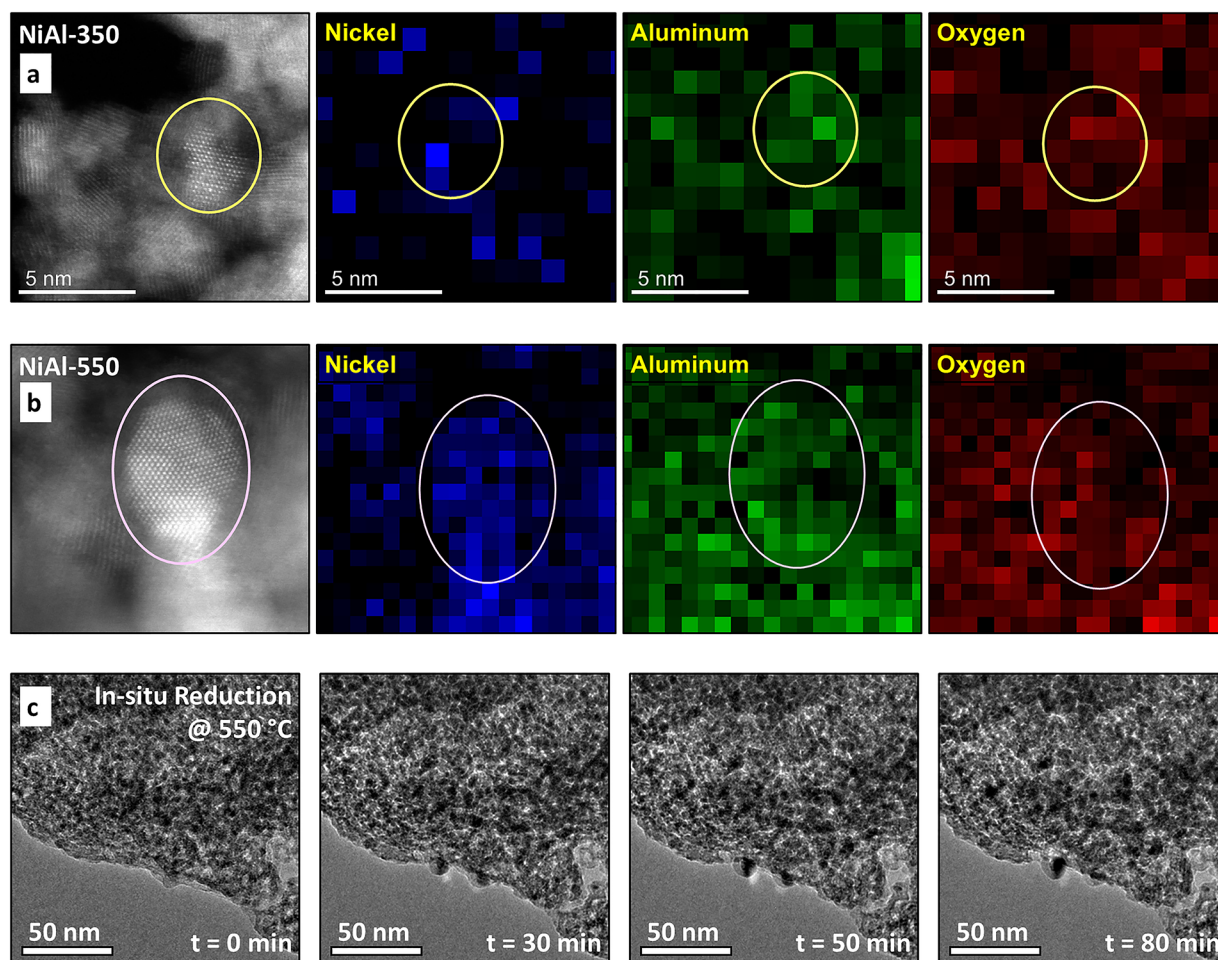
Figure 1. Electron microscopy of NiAl-T catalysts. (a) and (b) HAADF-STEM imaging with elemental mapping via EDS and EELS of NiAl-350 and NiAl-550, respectively. (c) ETEM of in-situ reduction of the calcined NiAl catalyst.

attributed to transformations associated with forming metallic Ni. Nickel cations dispersed across the surface and in subsurface layers must migrate together to undergo reduction and form segregated nanoparticles. Interestingly, increasing the reduction temperature to 550 °C diminishes the Ni^{2+}_{Td} peak intensity and grows the prominence of Ni^0, further indicating that Ni^{2+}_{Td} migrates into metallic Ni nanoparticles. The migration of cationic nickel species is corroborated by the O 1s spectra through the emergence of a shoulder at high binding energies, corresponding to oxygen of Al_2O_3[43] (Figure S3). The elemental concentrations from the XPS spectra indicate that the surface has an Al–Ni molar ratio of 9.0–10.5, corresponding to a surface Ni loading of 8–10 wt % (Table 1). The surface Ni loading is stable across the reduction treatments and much smaller than the bulk values attained from XRF, demonstrating the majority of Ni is tightly trapped deep within the bulk.

Surface species were also probed in-situ by infrared spectroscopy (IR). The differential IR spectra at 500 mTorr of CO in the range of 2300–1700 cm^{-1} are shown in Figure 2e. Notably, none of the IR spectra show strong bands in the 2210–2180 cm^{-1} region characteristic of CO adsorption on Al^{3+} sites,[44,45] suggesting that the high level of surface incorporation of Ni in the spinel structure quenches the Lewis acidity typically observed over alumina. CO adsorption over NiAl-250 and 350 only produces a single band at 2171

cm^{-1} assigned to CO complexes with Ni^{2+}_{Td},[44,46] with NiAl-350 having a higher intensity, indicating a larger fraction of these sites exposed at the surface. Interestingly, characteristic bands for Ni^{2+}_{Oh} at 2215–2205 cm^{-1}[44,46] are absent, revealing the octahedral Ni detected by XAS and XPS is in the subsurface layers and the bulk. The band at 2171 cm^{-1} is also present for NiAl-450 but the intensity is greatly reduced, and several peaks emerge at 2100–1900 cm^{-1}. Evacuation of CO to 10 mTorr shows that the bands at 2061 and 2044 cm^{-1} simultaneously decrease in intensity while bands at 2098 and 1940 cm^{-1} remain stable (Figure S4), indicating two chemical species. The former bands are assigned to atop adsorption of CO on NiO,[44,47,48] whereas the latter are indicative of irreversible binding of CO to metallic Ni.[44,48–50] We believe that the NiO species are likely located at the perimeter of the Ni nanoparticles and the oxide support. The trend in the fraction of tetrahedral Ni^{2+} cations across catalysts and the emergence of metallic Ni coincide with the XPS analysis, confirming that Ni^{2+}_{Td} serves as a migratory precursor to metallic Ni.

H_2 temperature-programmed reduction (TPR) can differentiate Ni^{2+} in various oxide environments and provide insights into the strength of the Ni–Al interactions.[29,30,51–53] TPR for nickel aluminates can be segregated into four types: Ni^{2+} in pure NiO (φ, 100–300 °C); Ni^{2+} in NiO weakly interacting with Al atoms (α, 350–550 °C); Ni^{2+} in NiO embedded in the Al_2O_3 matrix (β, 550–760 °C); and Ni^{2+} in the $NiAl_2O_4$ spinel
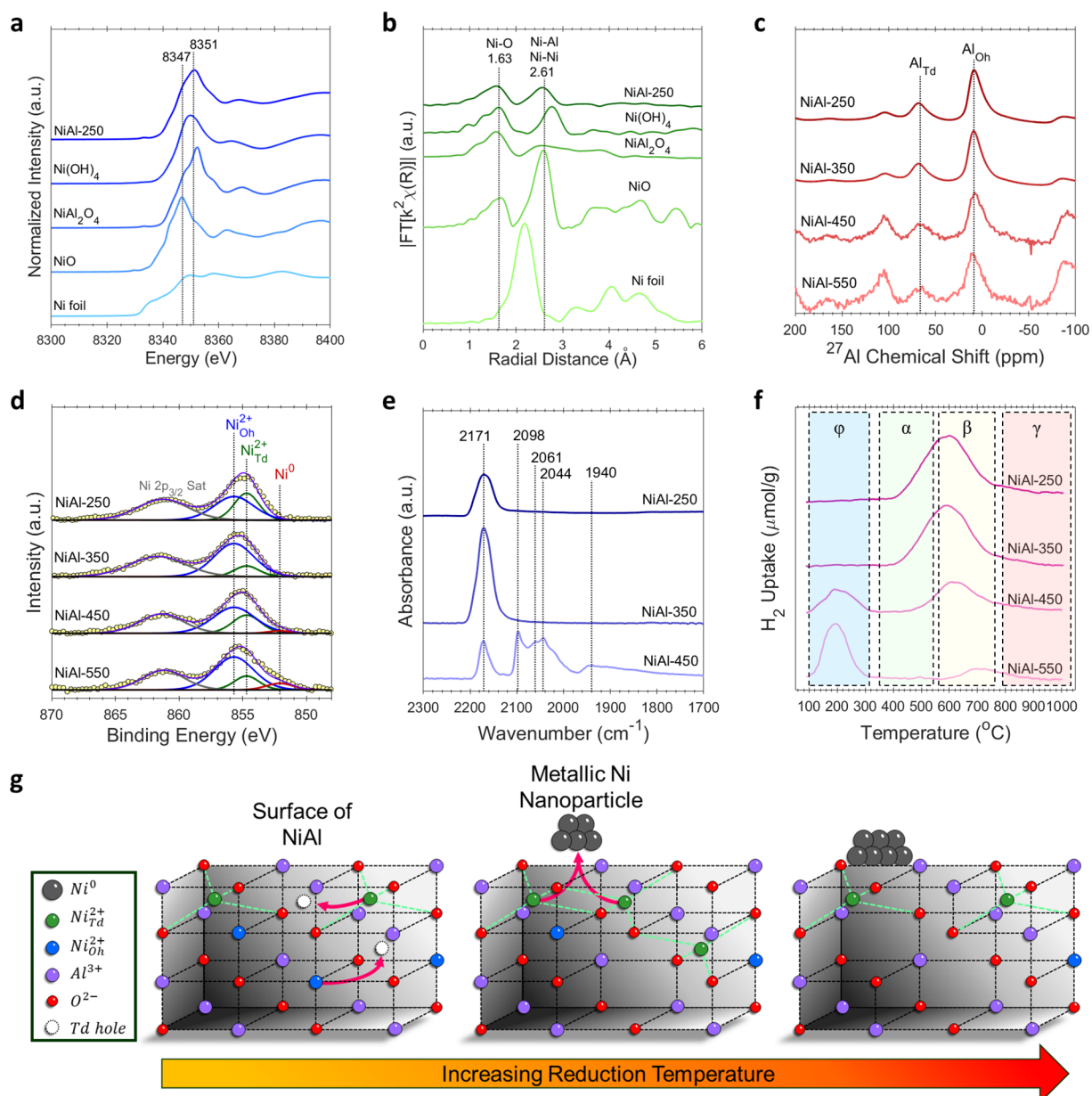
Figure 2. Catalyst characterization of the NiAl-T catalysts and reference standards: (a) XANES and (b) EXAFS analysis of XAS spectra, respectively. (c) ^{27}Al MAS NMR. (d) Air-free XPS. (e) IR of CO adsorption at 500 mTorr. (f) H_2 TPR with the temperature ranges highlighted for the various Ni^{2+} cations. (g) Conceptual schematic of the structural transformation and Ni nanoparticle generation in the near surface layers.

(γ, >800 °C).[29,32,51−53] Figure 2f shows the TPR of the NiAl-T catalysts after ex-situ reduction at the associated temperature and passivation in 1% O_2 at 30 °C. The TPR curves for NiAl-250 and 350 are similar, with one broad peak spanning 400−1000 °C and a maximum at ∼600 °C, demonstrating all Ni is present as Ni^{2+} cations strongly interacting with Al atoms, predominately as β-type NiO. The broadness of the H_2 uptake indicates a spectrum of Ni incorporation into the aluminum framework, corroborated by XRD (Figure S1) and XAS (Figure 2a,b). For NiAl-450 and 550, a new H_2 uptake peak is observed at 100−300 °C that is centered at ∼200 °C, corresponding to φ-type NiO, followed by a significant reduction in the H_2 uptake above 400 °C. Specifically for NiAl-550, the H_2 uptake maximum for β-type NiO shifts to ∼700 °C and the peak shape becomes left-skewed with a long tail into the γ-type range. The consumption of β-type NiO

concerted with the generation of φ-type NiO across the catalyst samples demonstrate reduction push of the Ni^{2+} incorporated in the alumina framework into metallic Ni nanoparticles that are oxidized into pure NiO upon passivation. Harsher reduction temperatures increase the amount of metallic Ni nanoparticles, but ∼24% of the detected Ni in NiAl-550 remains trapped in stoichiometric and nearly stoichiometric segments of nickel aluminates (i.e., γ-type Ni^{2+}). Furthermore, the consumed H_2 across all catalysts is likely used to reduce only surface Ni considering the Ni surface loading's stability from XPS.

Overall, the characterization methods provide a consistent picture. Ni nanoparticles form via the migration of cationic nickel in only the top few nanometers. This cationic nickel in the subsurface mostly resides as Ni^{2+}_{Oh}, but upon reaching the catalytic surface, it occupies tetrahedral sites (Ni^{2+}_{Td}). Ni^{2+}_{Td} then

agglomerates through surface diffusion and generates Ni nanoparticles upon reduction with H_2. Increasing the reduction temperature drives Ni to more metallic nanoparticles and disturbs the distribution of Ni in the subsurface layers (Figure 2g).

LDPE Hydrogenolysis over NiAl-T Catalysts

The NiAl-T catalysts were used for hydrogenolysis of LDPE ($M_w \sim 4$ kDa, Sigma-Aldrich) in a batch reactor at 300 °C and 30 bar H_2 to produce methane, liquid n-alkanes (C_6–C_{35}), and solid waxes ($C_{>35}$) as the main products. The performance after 2 h of reaction is shown in Figure 3a. NiAl-250 exhibited limited catalytic activity. Differential scanning calorimetry (DSC) of the solid residues and neat LDPE were similar and have an identical melting temperature (T_m) of 104.6 °C (Figure 3b), indicating slight changes of the solid. Increasing the reaction time to 14 h showed no changes in product yields or DSC curves. NiAl-350 and 450 showed the highest apparent activities and reduced the yield of the solid residue to ~55%, comparable to recently reported Ni/SiO_2,[14,15] while NiAl-550 was slightly less active yielding ~65% solids (Figure 3a). Full LDPE deconstruction was attained within 10 h of reaction on NiAl-350 (Figure S5). DSC of the solid residues after 2 h of reaction differ considerably from the neat LDPE and the primary T_m is reduced by 5–10 °C, indicating a significant reduction in the polymer molecular weight. Furthermore, the solids from NiAl-350 and 450 show a new melting peak at ~60 °C, corresponding to solid waxes.[15]

Pronounced differences are observed in the C_1–C_{35} carbon product selectivities across the active catalysts (Figure 3a). Astonishingly, NiAl-350 exhibited a <5% selectivity to methane, a 3–4× reduction compared to Ni/SiO_2[14,15] and comparable to the lowest selectivities attained by Ru-based catalysts.[9,12,13,17] This remarkable selectivity is maintained near full deconstruction of LDPE, where secondary reactions on the cracked products lead to additional methane (Figure S5). NiAl-450 and 550 displayed much higher methane selectivities of ~18 and ~33%, respectively, an overall sevenfold growth across the catalysts. Surprisingly, limited impact is observed on the generation of heavier hydrocarbons. The three catalysts have nearly identical shapes with lower yields in their product distributions across the liquid range and share a maximum near C_{22} (Figures 3c and S6). It was recently elucidated via the divergent hydrogenolysis mechanism[15] that LDPE hydrogenolysis is dominated by slow internal C–C scission followed by fast, terminal cascades on the adsorbed alkyl-species, responsible for generating methane. The wide disparity in the methane yield and relatively constant distribution of heavy alkanes indicate that only the rate of terminal C–C scission is being modified. The enhanced methane production across the catalyst is attributed to the redistribution of Ni cations in the subsurface. As characterization shows (Figure 2), increased reduction temperature draws more metallic Ni to the catalyst surface and changes the concentration of Ni_{Oh}^{2+} and Ni_{Td}^{2+} cations, but there is no clear trend with methane selectivity.

Catalysts have been well-documented to restructure under reaction conditions and throughout the course of a reaction.[54,55] This is certainly possible for our catalysts during LDPE hydrogenolysis as the reaction conditions encompass high H_2 pressures and temperatures. Subsequently, post-reaction characterization of the NiAl-T catalysts was undertaken to further elucidate the cause of the varying methane selectivity. The NiAl-T catalysts were collected after long-
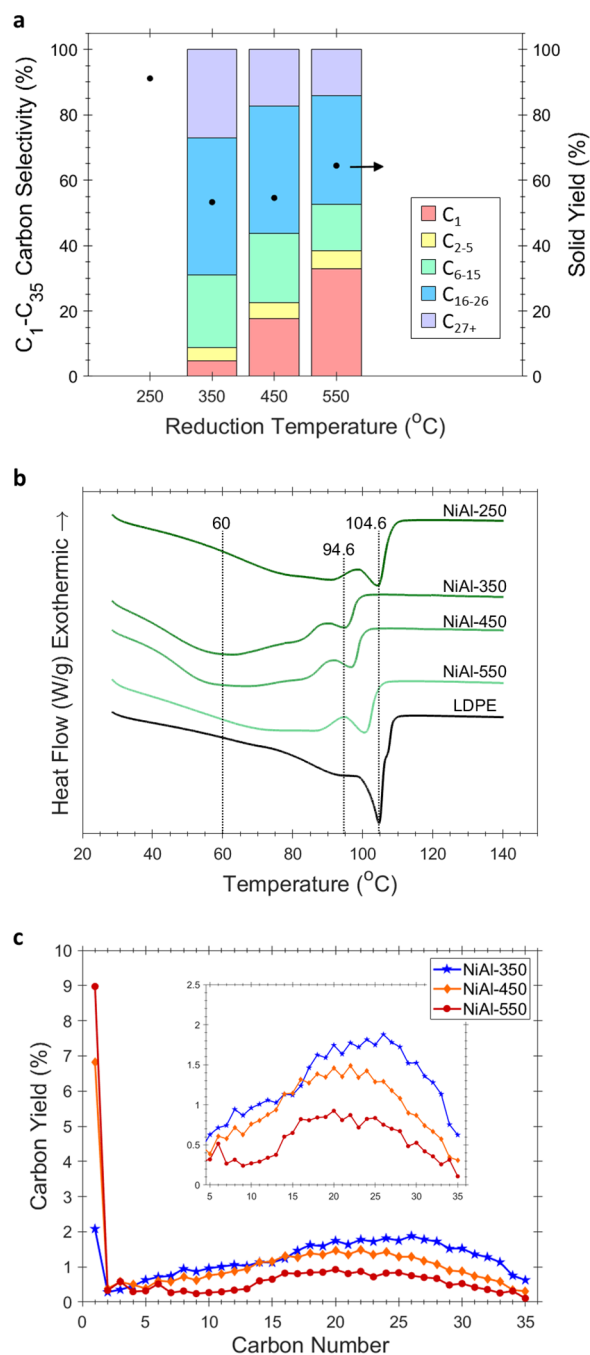

Figure 3. LDPE hydrogenolysis results using the NiAl-T catalysts. (a) C_1–C_{35} carbon selectivities and yield of solid for each catalyst. (b) DSC curves of the solid residues and the neat LDPE. (c) Carbon product distribution for three active catalysts. The inset shows a magnification from C5 to C35 carbons. Reaction conditions: 2.0 g LDPE ($M_w \sim 4$ kDa), 200 mg NiAl-T, 300 °C, and 30 bar H_2 for 2 h.

duration (14 h) LDPE hydrogenolysis reactions in a glovebox to prevent spontaneous oxidation with ambient air. Figure 4a shows the air-free XPS of NiAl-350, 450, and 550 after LDPE hydrogenolysis. Expectedly, the XPS spectra of the spent catalysts are quite different from the fresh catalysts. The Ni $2p_{3/2}$ spectra of the spent catalysts show metallic Ni (Ni^0) as either a shoulder or a well-defined peak at 852.1 eV, even over NiAl-350, demonstrating in-situ generation of Ni^0 under reaction conditions. Conversely, NiAl-250 showed no Ni^0 formation (Figure S7) and no activity (Figure 3), revealing
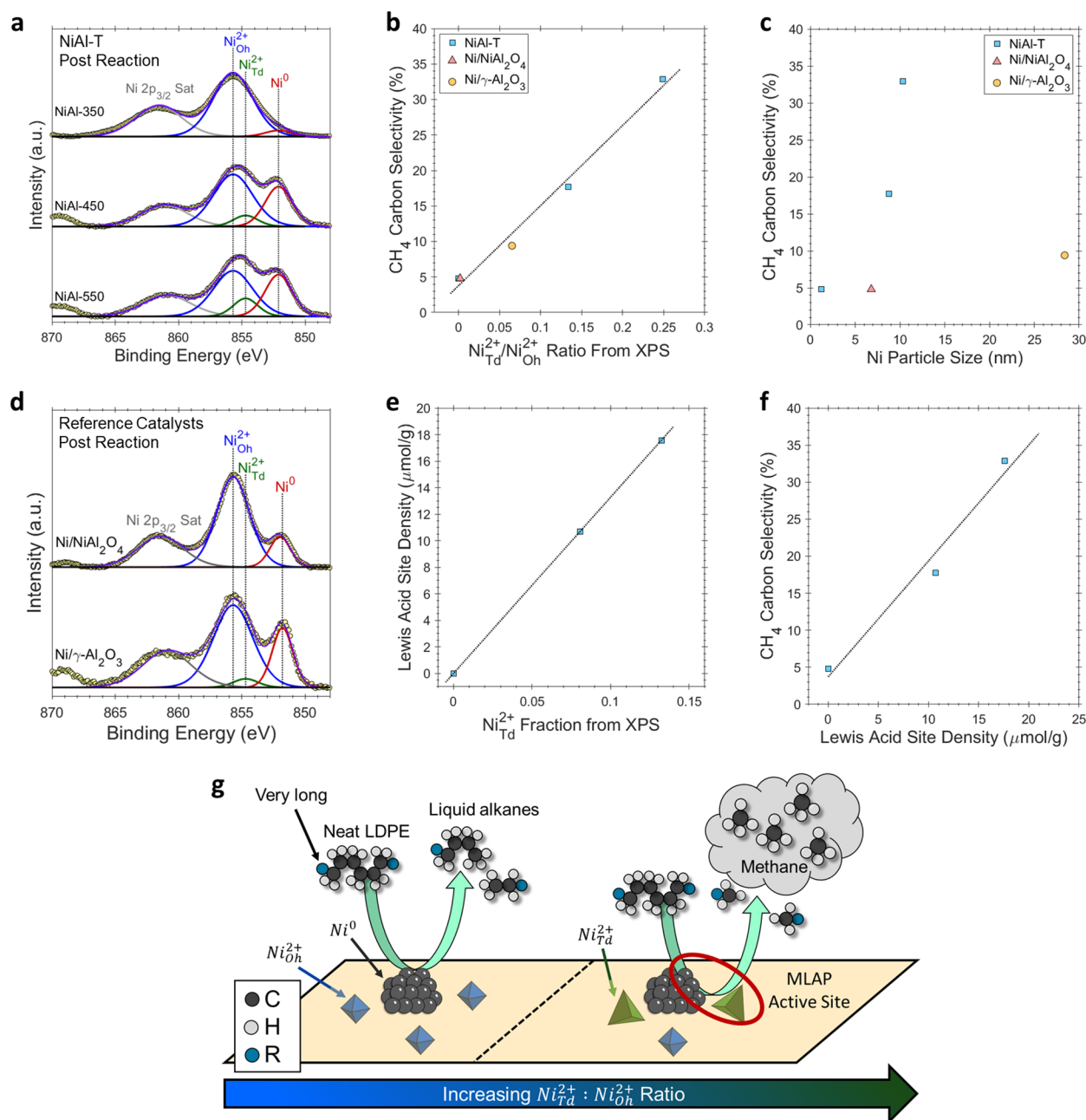
Figure 4. Characterization and analysis of the NiAl-T and reference catalysts after LDPE hydrogenolysis. (a) Air-free XPS spectra of the Ni $2p_{3/2}$ region from the NiAl-T catalysts. (b) Methane selectivity as a function of the tetrahedral and octahedral cationic Ni ratio. (c) Methane selectivity as a function of Ni nanoparticle size. (d) Air-free XPS spectra of the Ni $2p_{3/2}$ region from the Ni/NiAl$_2$O$_4$ and Ni/γ-Al$_2$O$_3$ reference catalysts. (e) LAS density from the spent NiAl-T catalysts as a function of the tetrahedral cationic Ni fraction. (f) Methane selectivity as a function of the spent NiAl-T catalyst LAS density. (g) Conceptual picture of the proposed mode by which Ni$_{Td}^{2+}$ *promotes methane production. Selectivity comparisons are made at 25−45% LDPE deconstruction.*

that Ni nanoparticles facilitate hydrogenolysis. Furthermore, deconvolution of the cationic Ni peak centered at ~855 eV demonstrates redistribution of Ni^{2+} between octahedral and tetrahedral coordinated sites. Similar to the fresh catalyst spectra, Ni$_{Oh}^{2+}$ is the dominant cationic species in all samples, but Ni$_{Td}^{2+}$ grows monotonically across catalysts. Methane selectivity as a function of the Ni$_{Td}^{2+}$/Ni$_{Oh}^{2+}$ ratio from XPS and the Ni particle size from N$_2$O titration[56] are shown in Figure 4b,c, respectively. Astonishingly, the ratio of the cationic Ni species and the methane selectivity correlate linearly (Figure 4b), indicating a structure−property relationship. N$_2$O titration (Figure 4c) of the spent NiAl-350 indicates a high

Ni dispersion, leading to small nanoparticles of 1.2 nm. The spent NiAl-450 and 550 have larger particles of 9 and 10 nm, respectively, demonstrating a growth in particle size after reaction but relatively comparable to those of the fresh materials. Cumulatively, these measured particle sizes show a potential asymptotic correlation with methane selectivity (Figure 4b) and suggest an alternative performance-controlling relationship.

Nickel impregnated onto gamma alumina (Ni/γ-Al$_2$O$_3$) and stoichiometric nickel aluminate (Ni/NiAl$_2$O$_4$) were used as reference catalysts to further probe these trends. Characterization shows that the physical properties of the reference

catalysts directly after reduction are similar to the coprecipitated NiAl-T catalysts. Briefly, air-free XPS (Figure S8) shows a mixture of Ni^0, Ni_{Oh}^{2+}, and Ni_{Td}^{2+} for Ni/γ-Al_2O_3, whereas Ni/$NiAl_2O_4$ is only composed of Ni^0 and Ni_{Oh}^{2+}. The presence of cationic Ni species in Ni/γ-Al_2O_3 is evident of Ni migrating into the alumina framework upon calcination and reduction treatments to form $Ni_xAl_yO_z$, as reported previously.[37,38,57] The Ni chemical environment is corroborated by XRD and H_2 TPR (Figure S9). N_2O titration indicates that Ni/Al_2O_4 has 6 nm Ni nanoparticles, comparable to the NiAl-T catalysts. Conversely, Ni/γ-Al_2O_3 has significantly larger nanoparticles of 28 nm determined by TEM (Figure S10) as the N_2O uptake was not appreciable.

The methane selectivity of Ni/$NiAl_2O_4$ and Ni/γ-Al_2O_3 was 4.8 and 9.4% (Figure S11), respectively, comparable to NiAl-350 and -450 at similar solid yields. The air-free XPS spectra of the reference catalysts also change after LDPE hydrogenolysis with metallic Ni becoming more pronounced; however, changes to the Ni_{Td}^{2+} and Ni_{Oh}^{2+} fractions were miniscule (Figure 4d). The Ni nanoparticle size for Ni/$NiAl_2O_4$ remained fairly stable (7 nm), whereas Ni/γ-Al_2O_3 remained unchanged. The selectivity of the reference catalysts falls onto the same linear trend between the $Ni_{Td}^{2+}/Ni_{Oh}^{2+}$ ratio and methane selectivity seen by the NiAl-T catalysts (Figure 4b), elucidating a lack of trend with a Ni particle size in the range of 1−30 nm (Figure 4c). These results further suggest a fundamental structure−property relationship for nickel−alumina catalysts, where decreasing the $Ni_{Td}^{2+}/Ni_{Oh}^{2+}$ ratio greatly reduces the methane generation (Figure 4b).

The mode by which the $Ni_{Td}^{2+}/Ni_{Oh}^{2+}$ ratio is controlling the LDPE hydrogenolysis methane selectivity is perplexing. The catalyst surface's H_2 storage capacity has been shown to significantly affect Ru-based catalysts,[13,17] but Al_2O_3 and $NiAl_2O_4$ are nonreducible supports as negligible differences are observed in the H_2 temperature-programmed desorption (TPD) of the NiAl-T and reference catalysts (Figure S12). Metal-support interactions, such as charge transfer, interfacial perimeter, and/or morphology could be responsible[58] but are unlikely. Al_2O_3 and $NiAl_2O_4$ are poorly conductive and the Ni nanoparticles are above the size threshold (max 5 nm) for charge transfer effects to be significant. Interfacial perimeter effects seem irrelevant because the selectivity does not scale with the particle size (Figure 4c). Additionally, the catalyst morphology is excluded as XRD shows negligible differences in the Ni crystalline phases across catalysts.

Subsequently, we hypothesize that changing the $Ni_{Td}^{2+}/Ni_{Oh}^{2+}$ ratio alters the intrinsic nature of the Ni active site, thus influencing the methane selectivity. Cryogenic CO IR demonstrated that a fraction of the Ni_{Td}^{2+} is present at the catalyst surface and agglomerates to form metallic Ni, meaning that these Lewis acid sites (LAS) reside near the periphery of the metal nanoparticle. Such close proximity in these sites could generate metal-Lewis acid pairs (MLAPs) which have been demonstrated to promote catalytic rates for various hydrogenation chemistries.[59,60] Pyridine IR of the spent NiAl-T catalysts detected negligible LAS density over NiAl-350, whereas NiAl-450 and 550 had LAS densities of 11 and 18 $\mu mol/g_{cat}$. Brønsted acid sites were not observed over the NiAl-T catalysts, rationalizing the limited isomerization of the hydrogenolysis products. Plotting the LAS density as a function of Ni_{Td}^{2+} fraction from XPS (Figure 4e) shows a linear correlation, validating the Ni_{Td}^{2+} sites as the source of Lewis acidity. Furthermore, the propensity to form MLAPs and their influence on the catalyst performance is confirmed by the strong linear correlation between the methane selectivity and LAS density (Figure 4f). We hypothesize that these MLAPs enhance the ability of the nickel aluminate catalysts to hydrogenate the alkyl chains, increasing the rate of C−C bond scission, the prevalence of terminal cascades, and promoting methane generation (Figure 4g). Alternatively, MLAPs could bind alkyl species tighter to the surface without altering C−C scission rates to have the same effect, based on the divergent hydrogenolysis mechanism.[15]

The presence or influence of MLAP sites has not been identified over nickel−alumina catalysts used in model alkane hydrogenolysis as harsh reaction conditions were used to fully reduce Ni^{2+} cations and prior studies prioritized the kinetics of these catalysts.[61−64] Alternatively, the selectivity control of cationic and metallic Ni has been elucidated in glycerol hydrogenolysis and methane steam reforming. In glycerol hydrogenolysis, cationic Ni facilitates dehydration routes, whereas metallic Ni preferentially targets direct dehydrogenation pathways.[32,33] Cationic Ni in methane steam reforming facilitates dry reforming reaction to resist coke formation, while metallic sites catalyze the steam reforming of methane.[29,65] Nonetheless, these studies have neither differentiated the roles on octahedral and tetrahedrally coordinated Ni^{2+} cations nor identified the cooperative role of the Ni_{Td}^{2+} sites with Ni^0 to generate MLAPs and the associated changes in selectivity.

■ DISCUSSION

Here, we have demonstrated coprecipitated nickel aluminate (NiAl-T) catalysts to be active for LDPE hydrogenolysis and identified that ex-situ reduction treatments can tune the methane selectivity by nearly sevenfold (reduction from 33 to <5%). Characterization of the NiAl-T catalysts prior to reaction elucidates the mechanism for Ni nanoparticle formation. Cationic Ni in the near subsurface layers migrates to the catalytic surface as tetrahedral sites (Ni_{Td}^{2+}) before coalescing and undergoing reduction to metallic nanoparticles. Altering the catalyst reduction temperature between 350 and 550 °C alters the distribution and fraction of Ni in the subsurface layers. Air-free XPS of the spent catalysts reveals restructuring of the surface and subsurface which is dictated by the state of the catalyst after ex-situ reduction. Excitingly, XPS of the spent catalyst identified a strong linear correlation between the $Ni_{Td}^{2+}/Ni_{Oh}^{2+}$ ratio and methane selectivity, underscoring a tunable structure−property relationship where lower Ni_{Td}^{2+} fractions result in low methane selectivities. Metallic Ni nanoparticles appear as prerequisites for hydrogenolysis. Pyridine IR identified the generation of Lewis acid sites corresponding to surface Ni_{Td}^{2+} species, which are found at the periphery of the metallic Ni nanoparticles based on the mechanism for nanoparticle formation. These two sites form metal-Lewis acid pair (MLAPs) sites that are responsible for excessive methane generation. We hypothesize MLAPs enhance the direct hydrogenolysis rate of terminal C−C bonds or increase the binding strength of alkyl species to the catalyst surface, both of which increase the depth of terminal cascades and promote methane formation.

■ ASSOCIATED CONTENT

ⓢ Supporting Information

The Supporting Information is available free of charge at https://pubs.acs.org/doi/10.1021/jacsau.3c00232.

Full details of the experimental methodology and supplemental reaction and characterization data (PDF)

■ AUTHOR INFORMATION

Corresponding Author

Dionisios G. Vlachos − *Center for Plastics Innovation, University of Delaware, Newark, Delaware 19716, United States; Department of Chemical and Biomolecular Engineering, University of Delaware, Newark, Delaware 19716, United States;* ⊙ orcid.org/0000-0002-6795-8403; Email: vlachos@udel.edu

Authors

Brandon C. Vance − *Center for Plastics Innovation, University of Delaware, Newark, Delaware 19716, United States; Department of Chemical and Biomolecular Engineering, University of Delaware, Newark, Delaware 19716, United States*

Sean Najmi − *Center for Plastics Innovation, University of Delaware, Newark, Delaware 19716, United States*

Pavel A. Kots − *Center for Plastics Innovation, University of Delaware, Newark, Delaware 19716, United States;* ⊙ orcid.org/0000-0003-3582-4600

Cong Wang − *Center for Plastics Innovation, University of Delaware, Newark, Delaware 19716, United States;* ⊙ orcid.org/0000-0002-0451-344X

Sungho Jeon − *Department of Materials Science and Engineering, University of Pennsylvania, Philadelphia, Pennsylvania 19104, United States*

Eric A. Stach − *Department of Materials Science and Engineering, University of Pennsylvania, Philadelphia, Pennsylvania 19104, United States;* ⊙ orcid.org/0000-0002-3366-2153

Dmitri N. Zakharov − *Center for Functional Nanomaterials, Brookhaven National Laboratory, Upton, New York 11973, United States*

Nebojsa Marinkovic − *Department of Chemical Engineering, Columbia University, New York, New York 10027, United States*

Steven N. Ehrlich − *National Synchrotron Light Source, Brookhaven National Laboratory, Upton, New York 11973, United States*

Lu Ma − *National Synchrotron Light Source, Brookhaven National Laboratory, Upton, New York 11973, United States*

Complete contact information is available at:
https://pubs.acs.org/10.1021/jacsau.3c00232

Author Contributions

B.C.V.: Conceptualization, Methodology, Investigation, Formal analysis, Writing - original draft, review & editing. S.N.: Investigation, Formal Analysis, Writing − review & editing. P.A.K.: Investigation, Formal analysis, Writing - review & editing. C.W.: Formal analysis. S.J.: Investigation. E.A.S.: Supervision. D.N.Z. Investigation. N.M.: Investigation. S.N.E.: Investigation L.M. Supervision. D.G.V.: Writing - review & editing, Project administration, Funding acquisition. CRediT: **Brandon C. Vance** conceptualization, data curation, formal analysis, investigation, methodology, writing-original draft, writing-review & editing; **Sean Najmi** formal analysis, investigation, writing-review & editing; **Pavel A. Kots** formal analysis, investigation, writing-review & editing; **Cong Wang** formal analysis; **Sungho Jeon** investigation; **Eric A. Stach** supervision; **Dmitri N Zakharov** investigation; **Nebojsa S. Marinković** investigation; **Steven N. Ehrlich** investigation; **Lu Ma** supervision; **Dionisios G. Vlachos** funding acquisition, project administration, writing-review & editing.

Notes

The authors declare no competing financial interest.

■ ACKNOWLEDGMENTS

■ REFERENCES

(1) OECD. *Global Plastics Outlook*; 2022.

(2) Geyer, R.; Jambeck, J. R.; Law, K. L. Production, Use, and Fate of All Plastics Ever Made. *Sci. Adv.* **2017**, *3*, No. e1700782.

(3) European Bioplastics. Nova-Institute Bioplastics Market Development Update 2020. *Eur. Bioplastics Org.* **2020**, 1−2.

(4) Thushari, G. G. N.; Senevirathna, J. D. M. Plastic Pollution in the Marine Environment. *Heliyon* **2020**, *6*, No. e04709.

(5) Rillig, M. C.; Kim, S. W.; Kim, T. Y.; Waldman, W. R. The Global Plastic Toxicity Debt. *Environ. Sci. Technol.* **2021**, *55*, 2717−2719.

(6) Shi, Q.; Tang, J.; Liu, R.; Wang, L. Toxicity in Vitro Reveals Potential Impacts of Microplastics and Nanoplastics on Human Health: A Review. *Crit. Rev. Environ. Sci. Technol.* **2022**, 3863−3895. Taylor & Francis

(7) Sangkham, S.; Faikhaw, O.; Munkong, N.; Sakunkoo, P.; Arunlertaree, C.; Chavali, M.; Mousazadeh, M.; Tiwari, A. A Review on Microplastics and Nanoplastics in the Environment: Their Occurrence, Exposure Routes, Toxic Studies, and Potential Effects on Human Health. *Mar. Pollut. Bull.* **2022**, *181*, No. 113832.

(8) Lange, J. P. Managing Plastic Waste-Sorting, Recycling, Disposal, and Product Redesign. *ACS Sustainable Chem. Eng.* **2021**, *9*, 15722−15738.

(9) Chen, L.; Meyer, L. C.; Kovarik, L.; Meira, D.; Pereira-Hernandez, X. I.; Shi, H.; Khivantsev, K.; Gutiérrez, O. Y.; Szanyi, J. Disordered, Sub-Nanometer Ru Structures on CeO 2 Are Highly

Efficient and Selective Catalysts in Polymer Upcycling by Hydrogenolysis. *ACS Catal.* **2022**, *12*, 4618−4627.

(10) Kots, P. A.; Xie, T.; Vance, B. C.; Quinn, C. M.; de Mello, M. D.; Boscoboinik, J. A.; Wang, C.; Kumar, P.; Stach, E. A.; Marinkovic, N. S.; Ma, L.; Ehrlich, S. N.; Vlachos, D. G. Electronic Modulation of Metal-Support Interactions Improves Polypropylene Hydrogenolysis over Ruthenium Catalysts. *Nat. Commun.* **2022**, *13*, 5186.

(11) Mason, A. H.; Motta, A.; Das, A.; Ma, Q.; Bedzyk, M. J.; Kratish, Y.; Marks, T. J. Rapid Atom-Efficient Polyolefin Plastics Hydrogenolysis Mediated by a Well-Defined Single-Site Electrophilic/Cationic Organo-Zirconium Catalyst. *Nat. Commun.* **2022**, *13*, 7187.

(12) Tamura, M.; Miyaoka, S.; Nakaji, Y.; Tanji, M.; Kumagai, S.; Nakagawa, Y.; Yoshioka, T.; Tomishige, K. Structure-Activity Relationship in Hydrogenolysis of Polyolefins over Ru/Support Catalysts. *Appl. Catal. B Environ.* **2022**, *318*, No. 121870.

(13) Wang, C.; Yu, K.; Sheludko, B.; Xie, T.; Kots, P. A.; Vance, B. C.; Kumar, P.; Stach, E. A.; Zheng, W.; Vlachos, D. G. A General Strategy and a Consolidated Mechanism for Low-Methane Hydrogenolysis of Polyethylene over Ruthenium. *Appl. Catal. B Environ.* **2022**, *319*, No. 121899.

(14) Zhao, Z.; Li, Z.; Zhang, X.; Li, T.; Li, Y.; Chen, X.; Wang, K. Catalytic Hydrogenolysis of Plastic to Liquid Hydrocarbons over a Nickel-Based Catalyst. *Environ. Pollut.* **2022**, *313*, No. 120154.

(15) Vance, B. C.; Kots, P. A.; Wang, C.; Granite, J. E.; Vlachos, D. G. Ni/SiO2 Catalysts for Polyolefin Deconstruction via the Divergent Hydrogenolysis Mechanism. *Appl. Catal. B Environ.* **2023**, *322*, No. 122138.

(16) Zichittella, G.; Ebrahim, A. M.; Zhu, J.; Brenner, A. E.; Drake, G.; Beckham, G. T.; Bare, S. R.; Rorrer, J. E.; Román-Leshkov, Y. Hydrogenolysis of Polyethylene and Polypropylene into Propane over Cobalt-Based Catalysts. *JACS Au* **2022**, *2*, 2259−2268.

(17) Wang, C.; Xie, T.; Kots, P. A.; Vance, B. C.; Yu, K.; Kumar, P.; Fu, J.; Liu, S.; Tsilomelekis, G.; Stach, E. A.; Zheng, W.; Vlachos, D. G. Polyethylene Hydrogenolysis at Mild Conditions over Ruthenium on Tungstated Zirconia. *JACS Au* **2021**, *1*, 1422−1434.

(18) Chen, L.; Zhu, Y.; Meyer, L. C.; Hale, L. V.; Le, T. T.; Karkamkar, A.; Lercher, J. A.; Gutiérrez, O. Y.; Szanyi, J. Effect of Reaction Conditions on the Hydrogenolysis of Polypropylene and Polyethylene into Gas and Liquid Alkanes. *React. Chem. Eng.* **2022**, *7*, 844−854.

(19) Liu, S.; Kots, P. A.; Vance, B. C.; Danielson, A.; Vlachos, D. G. Plastic Waste to Fuels by Hydrocracking at Mild Conditions. *Sci. Adv.* **2021**, *7*, No. eabf8283.

(20) Vance, B. C.; Kots, P. A.; Wang, C.; Hinton, Z. R.; Quinn, C. M.; Epps, T. H.; Korley, L. S. T. J.; Vlachos, D. G. Single Pot Catalyst Strategy to Branched Products via Adhesive Isomerization and Hydrocracking of Polyethylene over Platinum Tungstated Zirconia. *Appl. Catal. B Environ.* **2021**, *299*, No. 120483.

(21) Bin Jumah, A.; Anbumuthu, V.; Tedstone, A. A.; Garforth, A. A. Catalyzing the Hydrocracking of Low Density Polyethylene. *Ind. Eng. Chem. Res.* **2019**, *58*, 20601−20609.

(22) Kim, D.; Hinton, Z. R.; Bai, P.; Korley, L. S. T. J.; Epps, T. H., III; Lobo, R. F. Metathesis, Molecular Redistribution of Alkanes, and the Chemical Upgrading of Low-Density Polyethylene. *Appl. Catal. B Environ.* **2022**, *318*, No. 121873.

(23) Ellis, L. D.; Orski, S. V.; Kenlaw, G. A.; Norman, A. G.; Beers, K. L.; Román-Leshkov, Y.; Beckham, G. T. Tandem Heterogeneous Catalysis for Polyethylene Depolymerization via an Olefin-Intermediate Process. *ACS Sustainable Chem. Eng.* **2021**, *9*, 623−628.

(24) Hasan, M. M.; Batalha, N.; Fraga, G.; Ahmed, M. H. M.; Pinard, L.; Konarova, M.; Pratt, S.; Laycock, B. Zeolite Shape Selectivity Impact on LDPE and PP Catalytic Pyrolysis Products and Coke Nature. *Sustainable Energy Fuels* **2022**, *6*, 1587−1602.

(25) Selvam, E.; Kots, P. A.; Hernandez, B.; Malhotra, A.; Chen, W.; Catala-Civera, J. M.; Santamaria, J.; Ierapetritou, M.; Vlachos, D. G. Plastic Waste Upgrade to Olefins via Mild Slurry Microwave Pyrolysis over Solid Acids. *Chem. Eng. J.* **2023**, *454*, No. 140332.

(26) Maqsood, T.; Dai, J.; Zhang, Y.; Guang, M.; Li, B. Pyrolysis of Plastic Species: A Review of Resources and Products. *J. Anal. Appl. Pyrolysis* **2021**, *159*, No. 105295.

(27) Yao, L.; King, J.; Wu, D.; Chuang, S. S. C.; Peng, Z. Non-Thermal Plasma-Assisted Hydrogenolysis of Polyethylene to Light Hydrocarbons. *Catal. Commun.* **2021**, *150*, No. 106274.

(28) Kots, P. A.; Vance, B. C.; Vlachos, D. G. Polyolefin Plastic Waste Hydroconversion to Fuels, Lubricants, and Waxes: A Comparative Study. *React. Chem. Eng.* **2022**, *7*, 41−54.

(29) Jiménez-González, C.; Boukha, Z.; De Rivas, B.; González-Velasco, J. R.; Gutiérrez-Ortiz, J. I.; López-Fonseca, R. Behavior of Coprecipitated NiAl2O4/Al2O3 Catalysts for Low-Temperature Methane Steam Reforming. *Energy Fuels* **2014**, *28*, 7109−7121.

(30) Gil-Calvo, M.; Jiménez-González, C.; de Rivas, B.; Gutiérrez-Ortiz, J. I.; López-Fonseca, R. Effect of Ni/Al Molar Ratio on the Performance of Substoichiometric NiAl2O4 Spinel-Based Catalysts for Partial Oxidation of Methane. *Appl. Catal. B Environ.* **2017**, *209*, 128−138.

(31) Kwon, Y.; Eichler, J. E.; Mullins, C. B. NiAl2O4 as a Beneficial Precursor for Ni/Al2O3 catalysts for the Dry Reforming of Methane. *J. CO2 Util.* **2022**, *63*, No. 102112.

(32) Morales-Marín, A.; Ayastuy, J. L.; Iriarte-Velasco, U.; Gutiérrez-Ortiz, M. A. Nickel Aluminate Spinel-Derived Catalysts for the Aqueous Phase Reforming of Glycerol: Effect of Reduction Temperature. *Appl. Catal. B Environ.* **2019**, *244*, 931−945.

(33) Pamphile-Adrian, A. J.; Passos, F. B.; Florez-Rodriguez, P. P. Systematic Study on the Properties of Nickel Aluminate (NiAl2O4) as a Catalytic Precursor for Aqueous Phase Hydrogenolysis of Glycerol. *Catal. Today* **2022**, *394-396*, 499−509.

(34) Gousi, M.; Andriopoulou, C.; Bourikas, K.; Ladas, S.; Sotiriou, M.; Kordulis, C.; Lycourghiotis, A. Green Diesel Production over Nickel-Alumina Co-Precipitated Catalysts. *Appl. Catal. A Gen.* **2017**, *536*, 45−56.

(35) Goula, M. A.; Charisiou, N. D.; Papageridis, K. N.; Delimitis, A.; Pachatouridou, E.; Iliopoulou, E. F. Nickel on Alumina Catalysts for the Production of Hydrogen Rich Mixtures via the Biogas Dry Reforming Reaction: Influence of the Synthesis Method. *Int. J. Hydrogen Energy* **2015**, *40*, 9183−9200.

(36) Nikolopoulos, I.; Kogkos, G.; Kordouli, E.; Bourikas, K.; Kordulis, C.; Lycourghiotis, A. Waste Cooking Oil Transformation into Third Generation Green Diesel Catalyzed by Nickel − Alumina Catalysts. *Mol. Catal.* **2020**, *482*, No. 110697.

(37) Zhang, Z.; Wei, T.; Chen, G.; Li, C.; Dong, D.; Wu, W.; Liu, Q.; Hu, X. Understanding Correlation of the Interaction between Nickel and Alumina with the Catalytic Behaviors in Steam Reforming and Methanation. *Fuel* **2019**, *250*, 176−193.

(38) Li, G.; Hu, L.; Hill, J. M. Comparison of Reducibility and Stability of Alumina-Supported Ni Catalysts Prepared by Impregnation and Co-Precipitation. *Appl. Catal. A Gen.* **2006**, *301*, 16−24.

(39) Ravi, M.; Sushkevich, V. L.; van Bokhoven, J. A. Towards a Better Understanding of Lewis Acidic Aluminium in Zeolites. *Nat. Mater.* **2020**, *19*, 1047−1056.

(40) Kim, Y.; Kim, P.; Kim, C.; Yi, J. A Novel Method for Synthesis of a Ni/Al2O3 Catalyst with a Mesoporous Structure Using Stearic Acid Salts. *J. Mater. Chem.* **2003**, *13*, 2353−2358.

(41) Kathiraser, Y.; Thitsartarn, W.; Sutthiumporn, K.; Kawi, S. Inverse NiAl2O4 on LaAlO3-Al2O3: Unique Catalytic Structure for Stable CO2 Reforming of Methane. *J. Phys. Chem. C* **2013**, *117*, 8120−8130.

(42) Benrabaa, R.; Barama, A.; Boukhlouf, H.; Guerrero-Caballero, J.; Rubbens, A.; Bordes-Richard, E.; Löfberg, A.; Vannier, R. N. Physico-Chemical Properties and Syngas Production via Dry Reforming of Methane over NiAl2O4 Catalyst. *Int. J. Hydrogen Energy* **2017**, *42*, 12989−12996.

(43) Rotole, J. A.; Sherwood, P. M. A. Gamma-Alumina (γ-Al 2 O 3) by XPS. *Surf. Sci. Spectra* **1998**, *5*, 18−24.

(44) Hadjiivanov, K. I.; Vayssilov, G. N. Characterization of Oxide Surfaces and Zeolites by Carbon Monoxide as an IR Probe Molecule. *Adv. Catal.* **2002**, *47*, 307−511.

(45) Ballinger, T. H.; Yates, J. T., Jr. IR Spectroscopic Detection of Lewis Acid Sites on Al2O3 Using Adsorbed CO. Correlation with Al-OH Group Removal. *Langmuir* **1991**, *7*, 3041−3045.

(46) Borello, E.; Cimino, A.; Ghiotti, G.; Lo Jacono, M.; Schiavello, M.; Zecchina, A. Surface Configurations and Infra-Red Studies on Nickel Oxide Supported on *η* - and *γ* -Al 2 O 3. *Discuss. Faraday Soc.* **1971**, *52*, 149−160.

(47) Courtois, M.; Teichner, S. J. Infrared Studies of CO, O2, and CO2 Gases and Their Interaction Products, Chemically Adsorbed on Nickel Oxide. *J. Catal.* **1962**, *1*, 121−135.

(48) Vogt, C.; Kranenborg, J.; Monai, M.; Weckhuysen, B. M. Structure Sensitivity in Steam and Dry Methane Reforming over Nickel: Activity and Carbon Formation. *ACS Catal.* **2020**, *10*, 1428−1438.

(49) Anderson, J. A.; Daza, L.; Fierro, J. L. G.; Rodrigo, M. T. Influence of Preparation Method on the Characteristics of Nickel/Sepiolite Catalysts. *J. Chem. Soc., Faraday Trans.* **1993**, *19*, 3651−3657.

(50) Campuzano, J. C.; Greenler, R. G. The Adsorption Sites of CO on Ni(111) as Determined by Infrared Reflection-Absorption Spectroscopy. *Surf. Sci.* **1979**, *83*, 301−312.

(51) Koo, K. Y.; Roh, H. S.; Seo, Y. T.; Seo, D. J.; Yoon, W. L.; Bin Park, S. A Highly Effective and Stable Nano-Sized Ni/MgO−Al2O3 Catalyst for Gas to Liquids (GTL) Process. *Int. J. Hydrogen Energy* **2008**, *33*, 2036−2043.

(52) Zou, X.; Wang, X.; Li, L.; Shen, K.; Lu, X.; Ding, W. Development of Highly Effective Supported Nickel Catalysts for Pre-Reforming of Liquefied Petroleum Gas under Low Steam to Carbon Molar Ratios. *Int. J. Hydrogen Energy* **2010**, *35*, 12191−12200.

(53) Zhao, A.; Ying, W.; Zhang, H.; Ma, H.; Fang, D. Ni-Al2O3 Catalysts Prepared by Solution Combustion Method for Syngas Methanation. *Catal. Commun.* **2012**, *17*, 34−38.

(54) Patil, R. B.; House, S. D.; Mantri, A.; Yang, J. C.; McKone, J. R. Direct Observation of Ni-Mo Bimetallic Catalyst Formation via Thermal Reduction of Nickel Molybdate Nanorods. *ACS Catal.* **2020**, *10*, 10390−10398.

(55) Tao, F. (. F.); Crozier, P. A. Atomic-Scale Observations of Catalyst Structures under Reaction Conditions and during Catalysis. *Chem. Rev.* **2016**, *116*, 3487−3539.

(56) Tada, S.; Yokoyama, M.; Kikuchi, R.; Haneda, T.; Kameyama, H. N2O Pulse Titration of Ni/*α*-Al2O3 Catalysts: A New Technique Applicable to Nickel Surface-Area Determination of Nickel-Based Catalysts. *J. Phys. Chem. C* **2013**, *117*, 14652−14658.

(57) López-Fonseca, R.; Jiménez-González, C.; De Rivas, B.; Gutiérrez-Ortiz, J. I. Partial Oxidation of Methane to Syngas on Bulk NiAl2O4 Catalyst. Comparison with Alumina Supported Nickel, Platinum and Rhodium Catalysts. *Appl. Catal. A Gen.* **2012**, *437-438*, 53−62.

(58) van Deelen, T. W.; Hernández Mejía, C.; de Jong, K. P. Control of Metal-Support Interactions in Heterogeneous Catalysts to Enhance Activity and Selectivity. *Nat. Catal.* **2019**, *2*, 955−970. Nature Publishing Group

(59) Shimizu, K. I.; Onodera, W.; Touchy, A. S.; Siddiki, S. M. A. H.; Toyao, T.; Kon, K. Lewis Acid-Promoted Heterogeneous Platinum Catalysts for Hydrogenation of Amides to Amines. *ChemistrySelect* **2016**, *1*, 736−740.

(60) Noh, G.; Lam, E.; Bregante, D. T.; Meyet, J.; Šot, P.; Flaherty, D. W.; Copéret, C. Lewis Acid Strength of Interfacial Metal Sites Drives CH3OH Selectivity and Formation Rates on Cu-Based CO2 Hydrogenation Catalysts. *Angew. Chem., Int. Ed.* **2021**, *60*, 9650−9659.

(61) Kochloefl, K.; Bažant, V. Hydrogenolysis of Saturated Hydrocarbons on a Nickel Catalyst. I. Kinetics of Hydrogenolysis of Ethylcyclohexane and Reactivity of Alkylcyclohexanes. *J. Catal.* **1967**, *8*, 250−260.

(62) Kochloefl, K.; Bažant, V. Hydrogenolysis of Saturated Hydrocarbons on a Nickel Catalyst. II. Selectivity of Hydrogenolytic Cleavage of Some Aliphatic and Alicyclic Hydrocarbons and Their Reactivity. *J. Catal.* **1968**, *10*, 140−148.

(63) Matsumoto, H.; Saito, Y.; Yoneda, Y. Contrast between Nickel and Platinum Catalysts in Hydrogenolysis of Saturated Hydrocarbons. *J. Catal.* **1970**, *19*, 101−112.

(64) Matsumoto, H.; Saito, Y.; Yoneda, Y. The Classification of Metal Catalysts in Hydrogenolysis of Hexane Isomers. *J. Catal.* **1971**, *22*, 182−192.

(65) Rogers, J. L.; Mangarella, M. C.; D'Amico, A. D.; Gallagher, J. R.; Dutzer, M. R.; Stavitski, E.; Miller, J. T.; Sievers, C. Differences in the Nature of Active Sites for Methane Dry Reforming and Methane Steam Reforming over Nickel Aluminate Catalysts. *ACS Catal.* **2016**, *6*, 5873−5886.